

Characteristics of wall-shear stress fluctuations in shock wave and turbulent boundary layer interaction

Fulin Tong, Junyi Duan & Xinliang Li

To cite this article: Fulin Tong, Junyi Duan & Xinliang Li (2021) Characteristics of wall-shear stress fluctuations in shock wave and turbulent boundary layer interaction, Journal of Turbulence, 22:12, 761-783, DOI: [10.1080/14685248.2021.1974466](https://doi.org/10.1080/14685248.2021.1974466)

To link to this article: <https://doi.org/10.1080/14685248.2021.1974466>



Published online: 11 Sep 2021.



Submit your article to this journal [↗](#)



Article views: 183




View related articles [↗](#)



View Crossmark data [↗](#)



Characteristics of wall-shear stress fluctuations in shock wave and turbulent boundary layer interaction

Fulin Tong^{a,b,c}, Junyi Duan^{a,d} and Xinliang Li ^{a,d}

^aLHD, Institute of Mechanics, Chinese Academy of Sciences, Beijing, People's Republic of China; ^bState Key Laboratory of Aerodynamics, China Aerodynamics Research and Development Center, Mianyang, People's Republic of China; ^cComputational Aerodynamics Institute, China Aerodynamics Research & Development Center, Mianyang, People's Republic of China; ^dSchool of Engineering Science, University of Chinese Academy of Sciences, Beijing, People's Republic of China

ABSTRACT

The wall-shear stress (WSS) fluctuations in the interaction of an oblique shock wave with a flat-plate turbulent boundary layer are investigated by means of direct numerical simulation (DNS) at Mach 2.25. The numerical results agree very well with previous experiments and DNS data in terms of turbulence statistics, wall pressure, and skin friction. The fluctuating WSS characteristics, including probability density function (PDF), frequency spectrum, space–time correlation, and convection velocity, are analysed systematically. It is found that the positively skewed PDF shape of the streamwise WSS fluctuations is significantly changed due to the presence of a separation bubble, while the PDF shape of the spanwise component is slightly affected, exhibiting a symmetric behaviour across the interaction. The weighted power-spectrum density map indicates that the low-frequency unsteadiness associated with the separated shock - exhibits little influence on the spectrum for either component, and no enhancement of the low-frequency energy is observed. A significant reduction in the spatial extent of the two-point correlation is observed, causing spanwise elongated coherence for the streamwise WSS fluctuations in the separation region. Moreover, the elliptic behaviour of the space–time correlations is essentially preserved throughout the interaction, and this is accompanied by a sudden reduction of the convection velocity in the separation bubble.

ARTICLE HISTORY



Received 5 March 2021
Accepted 25 August 2021

KEYWORDS

Wall-shear stress; shock wave; turbulent boundary layers

1. Introduction

Due to its great significance and relevance in a variety of practical flows, shock wave and turbulent boundary layer interaction (SWTBLI) has been investigated both experimentally and numerically in the past few decades. Notable advances have been made on this topic, even though the physical mechanisms associated with the interaction are not fully

CONTACT Fulin Tong  515363491@qq.com  LHD, Institute of Mechanics, Chinese Academy of Sciences, 100190, Beijing, People's Republic of China; State Key Laboratory of Aerodynamics, China Aerodynamics Research and Development Center, 621000, Mianyang, People's Republic of China; Computational Aerodynamics Institute, China Aerodynamics Research & Development Center, 621000, Mianyang, People's Republic of China

understood. This is especially true of low-frequency unsteadiness and turbulence amplification, which have been of particular interest over the past 50 years. The remarkable review work by Clemens and Narayanaswamy [1] detailed possible mechanisms for the source of the low-frequency unsteadiness. Very recently, Fang *et al.* [2] provided a comprehensive summary of the turbulence amplification and proposed a new amplification mechanism to explain the high levels of turbulence seen in some experiments and numerical simulations.

Wall-pressure and shear-stress fluctuations in SWTBLI are of great importance for the engineering prediction of structural vibrations and sound radiation. In recent decades, a significant amount of progress has been made in the fluctuating wall pressure field in both experimental and numerical studies. Through a space–time analysis of experimental wall-pressure data, Bonnet [3] obtained the structural modifications induced by SWTBLI in the case of a supersonic compression ramp with an angle of 18° . Bernardini *et al.* [4] carried out a direct numerical simulation (DNS) study on the structure of wall pressure in the interaction of a normal shock wave and a turbulent boundary layer at Mach 1.3. The behaviour of the fluctuating wall pressure, including fluctuation intensities, space–time correlation, convection velocities, and frequency spectra, was quantitatively analysed across the interaction zone. However, to date, fluctuating wall-shear stress (WSS) has received extremely limited attention with respect to the wall pressure. To our knowledge, no relevant studies on the characteristics of the WSS fluctuations in SWTBLI have so far been reported.

Most previous studies in the fluctuating WSS field have been mainly confined to experimental and numerical investigations of low-speed wall-bounded flow. A large number of experiments examining turbulent duct flow, turbulent boundary layers, and cylindrical configurations are available in the well-accepted literature. Grosse and Schröder [5] experimentally investigated the two-dimensional WSS distribution in turbulent duct flow using the micro-pillar shear-stress sensor. They evidenced the wave-like patterns of the spanwise WSS fluctuations, as previously reported by Brücker [6], which were characterised by the occurrence of high streamwise shear regions and momentum transfer towards to the wall. Measurements of the WSS fluctuations in a zero pressure-gradient turbulent boundary layer (TBL) at $Re_\theta = 3150$ and 2160 were reported by Colella and Keith [7]. They found that the shape of the probability density function (PDF) was positively skewed, and the power spectral density (PSD) was found to scale with outer variables. Their experiments also showed that no flow reversal (negative value of the WSS) was observed at the wall. Similarly, Nottebrock *et al.* [8] noticed that the intensity, skewness, and kurtosis of the WSS were decreased due to the adverse pressure gradient effect. The instantaneous streamwise component of the WSS fluctuations on a cylinder surface were measured by Wietrzak and Lueptow [9], who emphasised the transverse curvature effect on the PDF and PSD of the fluctuating WSS. Their experiments revealed that the PDF distribution was similar to that of planar wall-bounded flow, but less energy at lower frequencies and more energy at higher frequencies were identified. Using the oscillating hot-wire sensing technique, Li *et al.* [10] experimentally analysed the space–time characteristics of the WSS in an axisymmetric separating/reattaching flow. They found that the convection speed of the WSS fluctuations was in agreement with that of the wall-pressure fluctuations.

The emergence of DNS has also contributed to better elucidation of the behaviour of the WSS fluctuations. By using a DNS database of turbulent channel flow, Jeon *et al.* [11] numerically obtained the convection velocity of the streamwise and spanwise components of the fluctuating WSS. The Reynolds-number dependence of WSS spectra was

numerically investigated by Hu *et al.* [12] using DNS of turbulent channel flow up to $Re_\tau = 1440$. The wall-shear spectra were found to collapse for $Re_\tau > 360$ under viscous scaling. In the recent DNS of a zero pressure-gradient TBL, Daniel *et al.* [13] focused on the relationship between the statistical moments of the filtered WSS fluctuations and the second-order structure function of fluctuating velocity inside the boundary layer. They argued that the slope of the velocity energy spectra might be effectively modified by the intermittency of the fluctuating WSS.

The aim of this paper is to characterise the structural and statistical properties of the unsteady WSS field by means of DNS. Up to now, there have been limited DNS studies of the fluctuating WSS in SWTBLI. For this reason, we present DNS of a 33.2° oblique shock wave and a flat-plate turbulent boundary layer at Mach 2.25 and $Re_\tau = 750$, with particular emphasis on two-point correlation, space-time correlation, and convection velocity. The inflow parameters are chosen to match the simulations of Fang *et al.* [2] Under such conditions, a large area of separation bubble and the large-scale low-frequency motion of the separated shock wave are induced by a mild adverse pressure gradient, from which substantial modifications of the fluctuating WSS across the interaction region are expected. The remainder of paper is organised as follows. In Section II, we provide the numerical methodology, together with a validation of the present results. In Section III, the characteristics of the WSS fluctuations are presented and discussed. Finally, conclusions are given in Section IV.

2. Direct numerical simulation

2.1. Numerical methodology

In the present simulation, we directly solve the full three-dimensional compressible Navier–Stokes equations with a perfect gas in a generalised curvilinear coordinate system that is non-dimensionalized by the free-stream parameters. The high-order finite-difference solver OpenCFD-SC used in our simulations has been successfully applied to many previous studies of compression ramps [14,15], impinging SWTBLIs over an expansion corner [16], and hypersonic transition [17]. The convective terms in the governing equations are discretized using a bandwidth-optimised fourth-order weighted essentially non-oscillatory (WENO) scheme, as proposed by Martin *et al.* [18], and the Steger–Warming vector flux splitting method. To properly resolve turbulence in the smooth region, the original WENO scheme is modified by using symmetric candidate stencils and a set of optimal WENO weights. As pointed out by Wu and Martin [19], the optimised numerical scheme is too dissipative to be employed in DNS of SWTBLI flows. With regard to this, we use a combination of an absolute limiter based on the WENO smoothness measurement and a relative limiter based on the total variation to greatly reduce the numerical dissipation, as suggested by Wu and Martin [19]. The diffusive terms are approximated using an eighth-order accurate central difference scheme, and the time integration is performed by means of a third-order Runge–Kutta method. The working fluid is assumed to be a perfect gas and the Sutherland’s law is applied to compute the molecular viscosity.

The inflow Mach number and static temperature are $M_\infty = 2.25$ and $T_\infty = 169.44$ K, respectively. Based on 99% of the inflow velocity U_∞ , the inflow boundary layer thickness is $\delta_i = 0.6$ mm. The Reynolds number $Re_{\delta_i} = \rho_\infty U_\infty \delta_i / \mu_\infty$ is estimated to be 15 000,

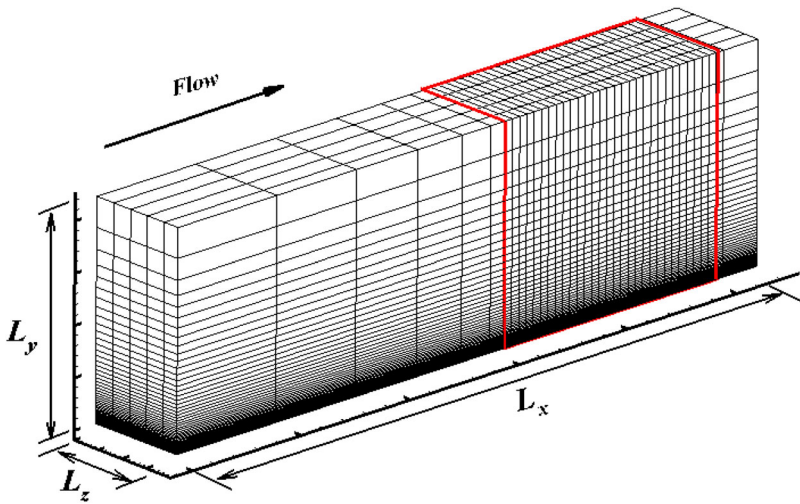


Figure 1. Illustration of the computational domain and grid for the DNS. The grid points are displayed with certain intervals for visualisation and the red box denotes the interaction region.

higher than the value used in recent DNS of Fang *et al.* [2] Note that, in this paper, the subscript ∞ denotes the free-stream parameter. For DNS of SWTBLI, turbulent inflow generation is a critical issue. In our simulation, a laminar-to-turbulent method, as widely used in many early DNS studies of compressible TBLs [20,21], is applied. The basic idea is to generate a fully developed TBL through the transition induced by wall blowing and suction disturbances. The mean laminar inflow profile is obtained beforehand from an auxiliary flat-plate boundary layer simulation. A region of unsteady wall-normal velocity fluctuations, which is the same approach used by Pirozzoli *et al.* [20] and Fang *et al.*, [2] is introduced at the wall to trigger the transition. After the transition is completed, a fully developed TBL is established and impinged by the oblique shock wave in the downstream region.

2.2. Computational overview

A schematic view of the computational domain, which has dimensions $L_x \times L_y \times L_z = 229.3\delta_i \times 21.2\delta_i \times 7.3\delta_i$, is shown in Figure 1. This is discretized with a computational grid consisting of $N_x \times N_y \times N_z = 3700 \times 300 \times 250$ points. In the figure, the flow is from the left to the right, and the streamwise coordinate origin is located at the inlet. In the x direction, the domain is ideally divided into three typical regions, namely the transition zone, interaction zone, and sponge region. Here, 600 grid points are progressively refined in the transition region extending from $x = 0$ to $x = 106\delta_i$, which is succeeded by 3000 grid points uniformly distributed in the interaction region between $106\delta_i < x < 211.7\delta_i$. The sponge region from $x = 211.7\delta_i$ to $x = 229.3\delta_i$ contains 100 points, which are gradually coarsened to prevent the reflection of any disturbance from the outlet. In the y direction, the grid points are clustered towards the wall using a hyperbolic tangent mapping, which ensures that there are about 200 points inside the boundary layer in the interaction region.

Table 1. Boundary-layer parameters and grid resolutions at the reference station.

	Reynolds number			Grid spacing			
	Re_δ	Re_{δ^*}	Re_θ	Δx^+	Δy_w^+	Δy_e^+	Δz^+
Present DNS	51 087	11 840	3567	5.6	0.66	11.3	6.6
Fang <i>et al.</i> [2]	51 468	12 216	3700	7.7	0.73	12.5	5.6

In the spanwise direction, the grid points are distributed with a uniform spacing. Under such grid resolutions, the properties of the generated TBL at $x = 156.7\delta_i$ (denoted as the reference station hereafter) are in good agreement with the recent DNS findings of Fang *et al.*, [2] as listed in Table 1. Based on the viscous length scale $\delta_\nu = \nu_w/\mu_\tau$ (ν_w and μ_τ being the kinetic viscosity at the wall and the friction velocity, respectively), the grid spacing at the reference station is $\Delta x^+ = 5.6$ and $\Delta z^+ = 6.6$ in the streamwise and spanwise directions, respectively. In the wall-normal direction, the grid spacing varies from $\Delta y_w^+ = 0.66$ at the wall to $\Delta y_e^+ = 11.3$ at the edge of the boundary layer.

Throughout this paper, the variables δ , δ^* , and θ represent the nominal thickness, displacement thickness, and momentum thickness of the TBL at the reference station, respectively; the superscript ‘+’ denotes normalisation using the viscous length scale; and the subscripts ‘w’ and ‘e’ represent the variables at the wall and the edge of the boundary layer, respectively. Note that the selection of the domain width is critical to turbulence fluctuations in the spanwise direction. In many previous DNS studies of SWTBLI flow [22,23], it has been found that a width of twice the nominal TBL thickness at the reference station is enough. In our simulations, the spanwise width is set to be $L_z \approx 2.2\delta$, which is sufficiently wide. The spanwise two-point correlation of velocity fluctuations rapidly approaches zero as the spanwise distance increases to become $L_z/2$ (not reported here).

The computational domain is bounded by a laminar profile at the inlet and non-reflecting conditions with supersonic outflow boundary conditions at the outlet, as shown in Figure 2. At the bottom wall, no-slip and isothermal boundary conditions are applied, and the wall temperature is fixed at $T_w = 321.9$ K. The wall blowing and suction disturbance is enforced in the region $12.7\delta_i < x < 33.9\delta_i$ (indicated by a red line in Figure 2). Following Pirozzoli *et al.*, [20] Gao *et al.*, [24] and Fang *et al.*, [2] the normal disturbance velocity, defined as

$$v_{bs} = A_{bs}f_{bs}(x)g_{bs}(z)h_{bs}(t), \quad (1)$$

is enforced, with two modes in the perturbation function $f_{bs}(x)$, ten modes in $g_{bs}(z)$, and five modes in $h_{bs}(t)$. Detailed expressions of the perturbation functions $f_{bs}(x)$, $g_{bs}(z)$, and $h_{bs}(t)$ refer to the DNS of Fang *et al.* [2] To generate a fast transition to turbulence, the disturbance intensity A_{bs} and fundamental frequency ω_{bs} are set to $A_{bs} = 0.2U_\infty$ and $\omega_{bs} = 0.628U_\infty/\delta$. At the upper boundary, non-reflecting conditions are used to minimise spurious disturbances reflected back into the domain. An oblique shock wave with a shock angle of $\beta = 33.2^\circ$ is introduced by applying the inviscid Rankine–Hugoniot jump conditions before and after the impinging location ($x_{sh} = 137\delta_i$), in which the geometries and effects of shock generators are not considered. Regarding homogeneity in the spanwise direction, periodic boundary conditions are applied.

After a washout time of approximately $136\delta/U_\infty$, or two flow-through times, 600 samples of the three dimensional instantaneous flow field taken at $\Delta t = 1.25\delta/U_\infty$ are

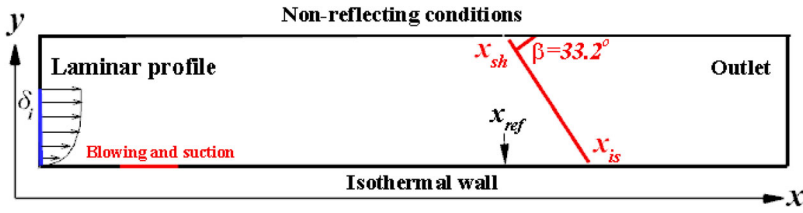


Figure 2. Boundary conditions for the DNS. The red line at the wall denotes the blowing and suction region.

averaged in time and in the spanwise direction to obtain statistical quantities. A total of 15 000 fully time-resolved WSS fields, covering $-5.5 < x^* < 12.5$ and $0 < z^* < 2.2$, are stored at constant sampling intervals of $\Delta t = 0.025\delta/U_\infty$ for a time period of $375\delta/U_\infty$ to guarantee statistical convergence.

2.3. Assessment of the DNS data

For validation, we first compare the properties of the generated incoming TBL with previous experimental data and numerical results in terms of the mean skin friction, mean velocity profile, and Reynolds stress components. In the following analysis, the Reynolds average and density-weighted average with a variable φ are defined as $\varphi = \bar{\varphi} + \varphi'$ and $\varphi = \bar{\varphi} + \varphi''$, respectively, where $\bar{\varphi} = \overline{\rho\varphi}/\bar{\rho}$. Here, the over bar denotes the average in the spanwise and in time.

A quantitative comparison of the mean skin friction coefficient at the reference location with that of Guarini *et al.*, [25] Maeder *et al.*, [26] and Schlatter and Orlu [27] is presented in Figure 3. For reference, the incompressible Blasius and Karman–Schoenherr algebraic relations are also included. The parameter $Re_{\theta,inc}$ is the Reynolds number based on the incompressible momentum thickness θ_{inc} . The extension to compressible flow is performed using the following van Driest II transformation:

$$C_{f,inc} = F_c C_f, Re_{\theta,inc} = F_\theta Re_\theta, \tag{2}$$

where

$$F_c = (\bar{T}_w/T_\infty - 1)/\arcsin^2 \alpha, \alpha = (\bar{T}_w/T_\infty - 1)/\sqrt{(\bar{T}_w/T_\infty)(\bar{T}_w/T_\infty - 1)},$$

$$F_\theta = \mu_\infty/\mu_w.$$

It is found that the present skin friction collapses well on the Karman–Schoenherr curve, but a small difference with 7% deviations from the Blasius curve is observed, confirming the accuracy of the present DNS. Figure 4(a) shows the van Driest transformed mean velocity at the reference station, defined as

$$U_{vd}^+ = u_\tau^{-1} \int_0^{\bar{u}_e} \sqrt{\frac{\bar{\rho}}{\bar{\rho}_w}} d\bar{u}. \tag{3}$$

The computed velocity profile agrees very well with the compressible DNS results of Fang *et al.* [2] for a similar Reynolds number, obeying the law of the wall in the near wall region for

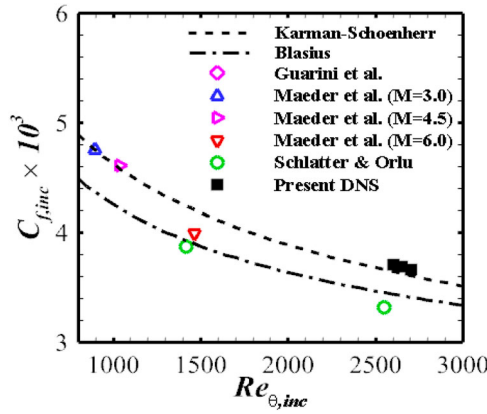


Figure 3. Distribution of transformed mean skin friction as a function of momentum thickness Reynolds number.

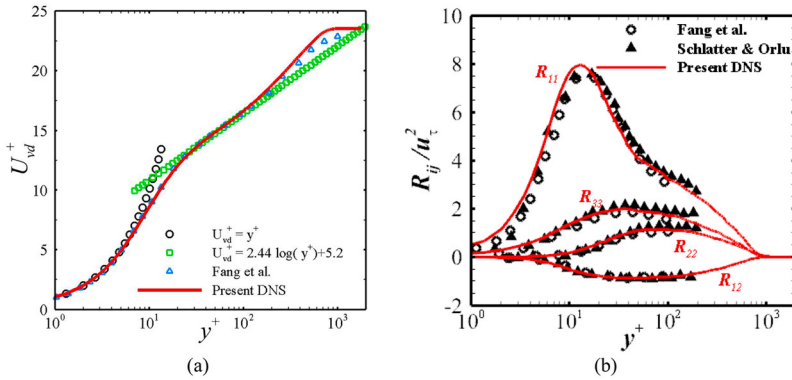


Figure 4. Turbulence statistics at x_{ref} : (a) Mean streamwise velocity U_{vd}^+ ; (b) Reynolds stress components $R_{ij} = (\bar{\rho}/\bar{\rho}_w)\widetilde{u''_i u''_j}$.

$y^+ < 10$ and the log law with constant $C = 5.2$ in the logarithmic region. In Figure 4(b), the density-scaled Reynolds stress components R_{ij} normalised with the square of the friction velocity are reported on a logarithmic scale. The agreement with the compressible DNS data of Fang *et al.* [2] and the incompressible DNS results of Schlatter and Orlu [27] is remarkable, further supporting Morkovin’s hypothesis. In particular, the streamwise component attains its peak value at about $y^+ = 13$.

More quantitative evidence is provided in Figure 5(a), where the mean wall pressure $(P_w - P_\infty)/(P_1 - P_\infty)$ is reported as a function of a non-dimensional longitudinal coordinate $x_{tr} = (x - x_{rs})/\delta$. Here, P_1 is the downstream pressure of the reflected shock, determined using the Rankine–Hugoniot jump conditions, and x_{rs} is the streamwise position of the reflected shock, defined as the position corresponding to $P_w = (P_1 + P_\infty)/2$. In good agreement with the DNS results of Fang *et al.*, [2] the mean wall pressure experiences a rapid increase in the interaction region, gradually approaching the inviscid solution

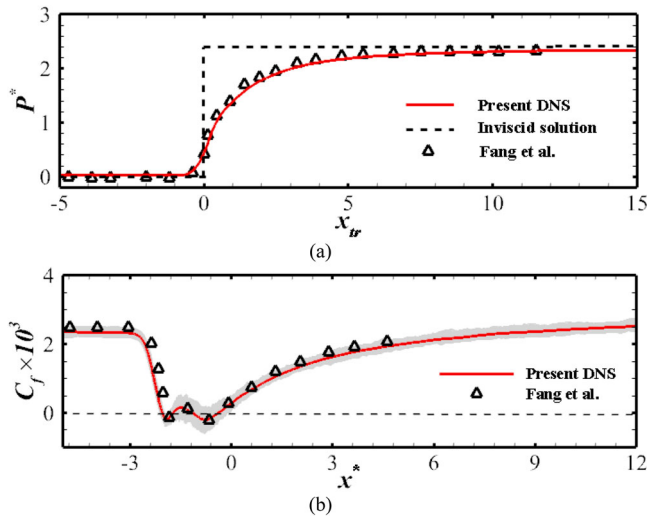


Figure 5. Distributions of (a) mean wall pressure and (b) mean skin-friction in the interaction region. The dashed line in (a) denotes the inviscid solution. The grey area in (b) represents the spanwise variation range of the time-average skin friction.

downstream of the interaction. Additionally, Figure 5(b) shows the mean skin-friction distribution together with the DNS data of Fang *et al.* [2]. For better comparison, the x axis is defined as $x^* = (x - x_{is})/\delta$ with x_{is} being the nominal impinging location of the oblique shock at the wall. In the interaction region, the figure highlights two separated regions (determined by the negative skin friction), a small region extending from $x^* = -2.03$ to $x^* = -1.71$ and another much larger region extending from $x^* = -1.21$ to $x^* = -0.35$, in very good agreement with the recent findings of Fang *et al.* [2]. In the remainder of this paper, the coordinates x^* and z^* ($z^* = z/\delta$) are used in the streamwise and spanwise directions, respectively.

3. Results and discussion

Figure 6 shows instantaneous structures in the interaction region. We observe that, after passing through the shock systems, the significantly strengthened vortex structures are lifted away from the wall due to the presence of a separated bubble induced by the adverse pressure gradient, and larger-scale vortices are massively concentrated in the outer part of the reattached boundary layer downstream, consistent with the observations of Fang *et al.* [2] and Pirozzoli and Grasso [28].

Figure 7 shows the contours of instantaneous streamwise and spanwise WSS fields in the x^*-z^* plane. Here, the streamwise and spanwise components of the fluctuating WSS, defined as

$$\tau'_x(x, z, t) = \mu \left. \frac{\partial u(t)}{\partial y} \right|_w - \overline{\mu \frac{\partial u(t)}{\partial y} \Big|_w}, \quad \tau'_z(x, z, t) = \mu \left. \frac{\partial w(t)}{\partial y} \right|_w - \overline{\mu \frac{\partial w(t)}{\partial y} \Big|_w}, \quad (4)$$

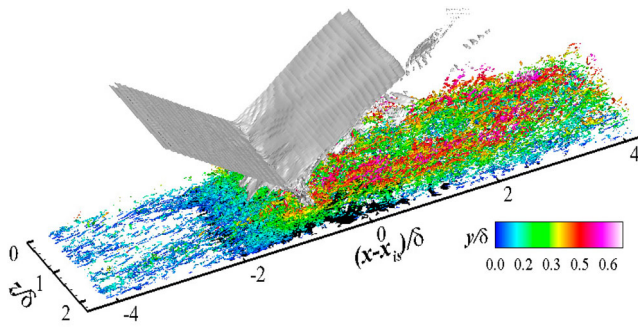


Figure 6. Instantaneous structures in the interaction region. The reversed flow in black is represented by the isosurface of $u = 0$, and the shock system is visualised by the pressure gradient modulus $|\nabla p| \delta/p_\infty = 100$. Coherent vortex structures are visualised by the iso-surface of Q equalling 1% of its global maximum and coloured with the wall-normal distance.

are considered in the present study. Note that the separation region is highlighted by the dashed and solid pink lines, corresponding to the mean separation point of the first separation bubble and the mean reattachment point of the second separation bubble, respectively. For τ_x , we see that the upstream TBL is characterised by typical streaky structures, as observed in low-speed experiments of turbulent duct flow and incompressible flat-plate TBL. These streaky structures disappear in the separation region, which is dominated by numerous patches of negative τ_x , and regenerate in the downstream region with larger spatial scales. Such behaviour closely resembles the variations of the near-wall velocity streaks across the interaction region, as found by Pirozzoli *et al.* [29] in transonic shock/boundary layer interaction and by Li *et al.* [30] in compression corner flow. However, the characteristics of the spanwise WSS in the interaction region are utterly different from those of τ_x . First, the spanwise component exhibits a wave-like pattern with an alternating sign in the upstream TBL, dominated by stronger meandering and smaller characteristic scales. Second, these structures are clearly preserved and frequently found with higher population density in the interaction region, which is indicative of enhancement of the wave-like pattern associated with shock interaction.

3.1. Probability density function

The PDFs of the streamwise WSS fluctuations, normalised by the root mean square (rms) at the reference station, are reported in Figure 8 using linear and logarithmic scales. These generally conform to the trend observed by incompressible experiments, [5–8] implying the compressibility effect is negligible. A satisfactory agreement with the compressible DNS data of Tong *et al.* [31] at Mach 2.9 and $Re_\theta = 2300$ is obtained, confirming a weak dependence on Reynolds number, as suggested by Hu *et al.* [12] in turbulent channel flow. The highly skewed PDF, having a longer positive tail, attains its peak at $\tau_x/\tau_{x,rms} \approx -0.5$. The use of the logarithmic scale in Figure 8(b), which is expected to emphasise the tail region, also highlights the occurrence of the reserved flow with small probability, as shown in the negative tail.

The normalised PDFs for both components of the fluctuating WSS at seven streamwise locations in the interaction region are shown in Figures 9 and 10, respectively.

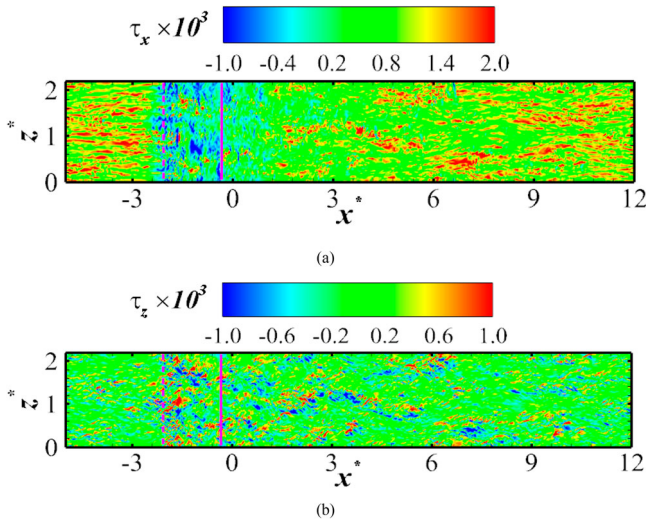


Figure 7. Contours of instantaneous WSS fields: (a) streamwise component τ_x ; (b) spanwise component τ_z .

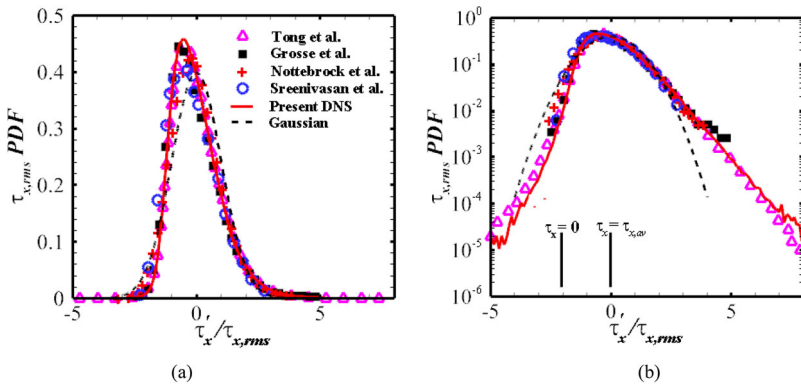


Figure 8. PDFs for the streamwise WSS fluctuations on (a) linear and (b) logarithmic scales at x_{ref} .

Here, three locations in the separation region, which are $x^* = -1.87$, $x^* = -1.50$, and $x^* = -0.75$, are denoted as S1–S3, respectively. The other four locations are $x^* = 1.67$, $x^* = 5.0$, $x^* = 8.34$, and $x^* = 11.63$, denoted as R1–R4 in the reattachment region, respectively. For the streamwise component, in the separation region, it is seen that the negative tails of the PDFs become much longer, whereas relatively slight differences are observed in the positive tails, resulting in a roughly symmetric distribution at locations S1–S3. This indicates that extreme negative fluctuations are more frequently observed as compared with the upstream TBL. In the reattachment region, the PDFs undergo a recovery process, with their peak locations shifting back to the value of the upstream TBL and their negative tails becoming smaller. This is likely to be associated with the regeneration of the streaky structures, as shown in Figure 7(a). At locations S3 and S4, the PDFs match well with that of the upstream TBL, suggesting this recovery is near

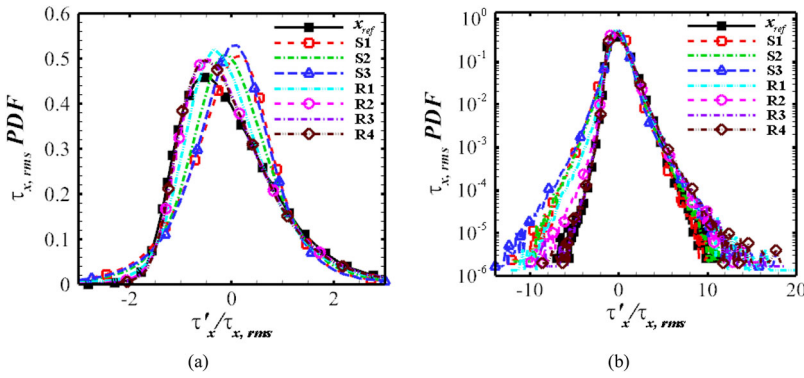


Figure 9. PDFs for the streamwise WSS fluctuations at various locations in the interaction region: (a) linear scale; (b) logarithmic scale.

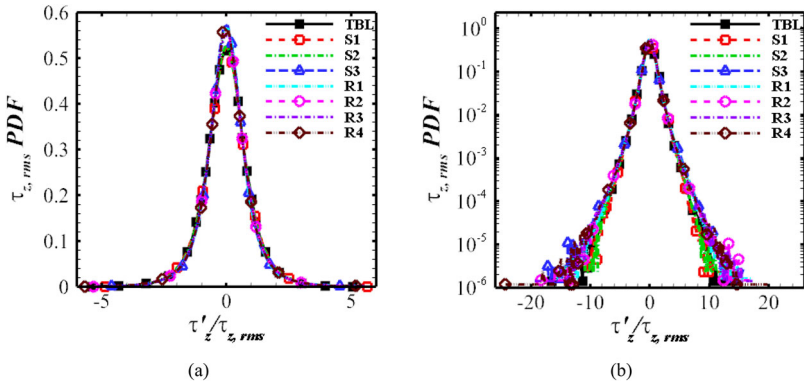


Figure 10. PDFs for the spanwise WSS fluctuations at various locations in the interaction region: (a) linear scale; (b) logarithmic scale.

completion. For the spanwise component, the PDFs for all locations are nearly symmetric, which is evidenced by the small skewness coefficient. A good collapse is apparently obtained in Figure 10, when the PDFs are normalised with their local rms values. It is suggested that the shock interaction does not essentially affect the PDFs of the spanwise WSS fluctuations.

3.2. WSS spectrum

The pre-multiplied energy spectra for both components at the reference station are shown in Figure 11, in which $\omega = 2\pi f$ is the angular frequency and $\Phi(\omega)$ is the PSD of the WSS fluctuations. Here the spectrum is normalised with respect to square of the mean streamwise WSS ($\tau^2_{x,av}$) and the inner reference time $\nu_w/u\tau^2$ is used. We decompose the overall fluctuating WSS signal into six segments with 50% overlaps, and the Welch’s method with a Hamming window is applied to estimate the spectra. It is found that the normalised spectra yield a very good collapse with the low-speed DNS data of Hu *et al.* [12] and Daniel *et al.*, [13] as well as the compressible DNS data of Tong *et al.*, [31] supporting the effectiveness of

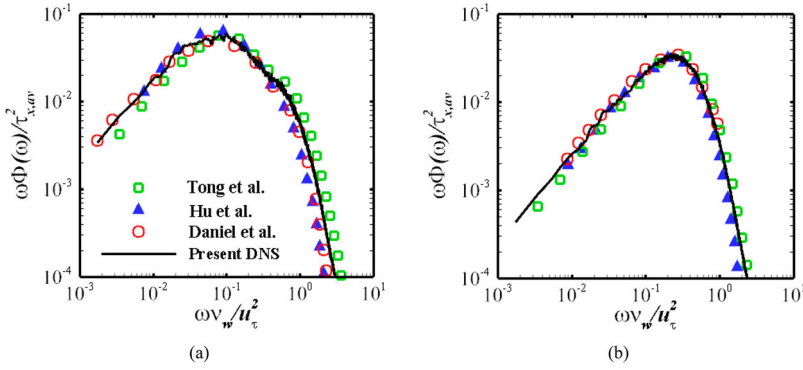


Figure 11. Pre-multiplied energy spectra for the WSS fluctuation at x_{ref} : (a) streamwise component τ_x ; (b) spanwise component τ_z .

the inner scaling. Clearly, the streamwise WSS spectrum peaks at about $\omega^+ \approx 0.09$, much lower than the value of $\omega^+ \approx 0.25$ for the spanwise component. As suggested by Daniel *et al.*, [13] it is presumably linked to the larger energy-containing scale for the streamwise WSS fluctuations.

To determine the effect of the unsteady shock motion on the WSS spectrum, Figure 12 shows the weighted PSD maps for the fluctuating WSS in the interaction region; the wall pressure spectrum is also shown for direct comparison. Following Pasquariello *et al.*, [32] the weighted PSD (WPSD) is defined as

$$WPSD = \omega\phi(\omega) / \int \phi(\omega)d\omega. \tag{5}$$

Note that the spectral map for wall pressure is plotted as a function of Strouhal number $St = f\delta/U_\infty$ for the convenience of explanation, rather than $\omega\nu_w/u_\tau^2$ used in the WSS spectrum. In Figure 12(a), the wall pressure spectrum exhibits close similarities to previous numerical and experimental findings for SWTBLI flows [33,34]. Upstream of the interaction, the spectra are mostly dominated by a broadband peak at about $St \approx O(1)$, which corresponds to the characteristic time scale of the most energetic structures in the fully developed TBL upstream. At the mean separation, the spectra are characterised by a dominating low-frequency peak around $St \approx O(10^{-2})$, which is an indication of the low-frequency unsteadiness associated with a separated shock wave. Downstream from the interaction, it is seen that this peak shifts towards higher frequencies due to the thickening of the reattached boundary layer.

However, the WSS spectra in Figure 12(b) and (c) highlight a completely different scenario. It is seen that the typical frequencies related to the upstream TBL are basically preserved across the interaction region, except that slight changes are observed in the separation region. It is important to note that, for both components, the low-frequency activity is obviously absent at the mean separation point and no more energy is observed in the lower-frequency range. It is believed that the fluctuating WSS in SWTBLI is almost insensitive to the low-frequency unsteady shock motion. A similar behaviour was also found by Bernardini *et al.* [35] in the case of SWTBLIs under different wall temperatures, who stated

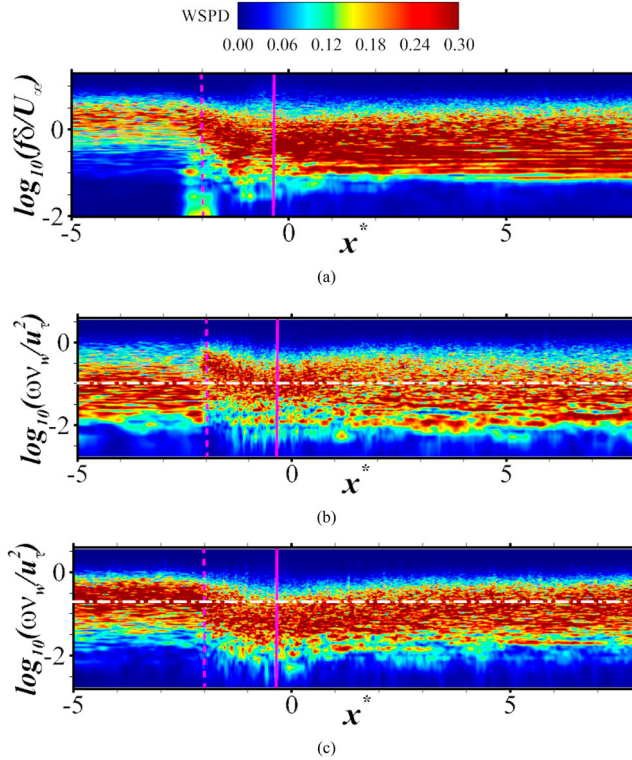


Figure 12. Weighted PSD map in the interaction region: (a) wall pressure; (b) streamwise WSS; (c) spanwise WSS. The pink dashed and solid lines denote the mean separation and reattachment points, respectively.

that the pre-multiplied spectra of wall heat flux do not show any evidence of influence from the low-frequency unsteadiness.

3.3. Space–time correlations

To gain a wealth of information regarding the spatial structure of the fluctuating WSS in the interaction region, two-point correlation maps for both components at various streamwise locations are directly compared with those of the upstream TBL. Similar to Bernardini and Pirozzoli [36], the two-point correlation of the WSS fluctuations is defined as

$$R_{\tau'\tau'}(x_0 : \Delta x, \Delta z) = \frac{\overline{\tau'(x_0, z, t)\tau'(x_0 + \Delta x, z + \Delta z, t)}}{\tau_{rms}(x_0)\tau_{rms}(x_0 + \Delta x)} \quad (6)$$

where Δx and Δz represent the streamwise and spanwise spatial separations, respectively, and x_0 is the reference probe. The correlation maps for the streamwise and spanwise components in the upstream TBL are given in Figure 13(a) and (b), respectively, where the spatial separations are normalised with the displacement thickness δ^* of the incoming TBL at x_{ref} to present the absolute value. In agreement with the findings of Grosse and Schröder [5] in incompressible turbulent duct flow and Tong *et al.* [31] in supersonic flat-plate TBL, the maps for both components are more elongated in the streamwise direction,

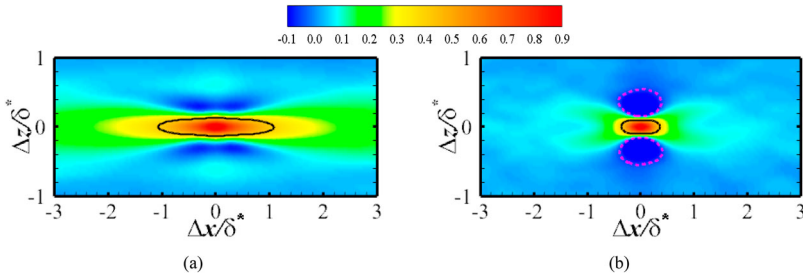


Figure 13. Two-point correlation maps of the fluctuating WSS at x_{ref} : (a) streamwise component τ_x ; (b) spanwise component τ_z . The solid and dashed lines denote correlation values of 0.3 and -0.1 , respectively.

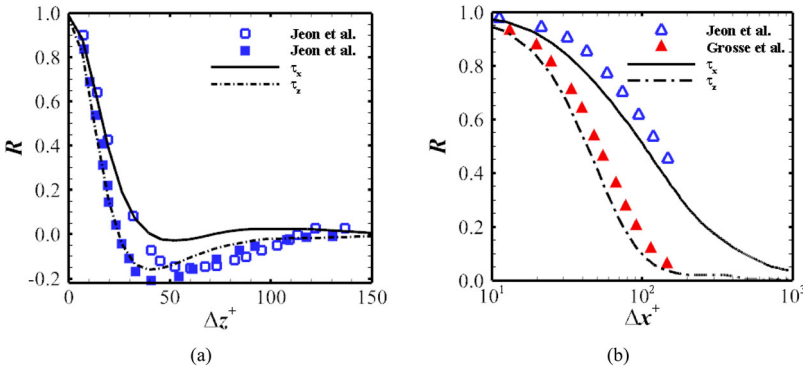


Figure 14. Profiles of the two-point correlation maps at x_{ref} : (a) spanwise profiles of $\Delta x = 0$; (b) streamwise profiles of $\Delta z = 0$.

especially for the large spatial separations, reflecting the increased anisotropic nature of the WSS field. The figures also reveal the occurrence of two negative-correlation regions flanking the central positive-correlation region, corresponding to the alternating pattern for the fluctuating WSS.

Notable quantitative differences can be identified from the streamwise and spanwise profiles of the two-point correlation map in Figure 14, in which low-speed experimental data from a turbulent duct [5] and incompressible DNS of channel flow [11] are also included. Despite there being relatively poor agreement due to different flow conditions, a distinct trend is still obtained in Figure 14(a). The spanwise profile attains its negative minimum at $\Delta z^+ \approx 50$ for the streamwise component and $\Delta z^+ \approx 40$ for the spanwise component, numerically corroborating the conclusions of Jeon *et al.* [11] in turbulent channel flow. For the streamwise profiles in Figure 14(b), the correlation drops rapidly with increasing streamwise distance, which is more significant for the spanwise component. Consistent with the experiments of Grosse and Schröder [5] and the DNS data of Jeon *et al.*, [11] the streamwise extent for the streamwise component is approximately $\Delta x^+ \approx \pm 500$ (at a correlation value of 0.1), rather larger than the value $\Delta x^+ \approx \pm 100$ for the spanwise component.

Figure 15 shows iso-lines of the two-point correlation maps for both components at various stations in the interaction region. Note that, for better visualisation, the axes in

the figure do not have the same scales. For the streamwise component, at location S1, the initial part of the separation region, the streamwise coherence is dramatically decreased, whereby a relative increase is observed in the spanwise coherence, thus leading to a highly spanwise-elongated contour shape. This is mainly attributed to the disappearance of the streaky structures. Further downstream, the spanwise-elongated contours at locations S2 and S3 become more pronounced, implying significantly enhanced spanwise coherence in the separation region. Such behaviour has also been observed in the two-point correlation maps of wall-pressure fluctuation inside a separation bubble by Na and Moin [37] and in the adverse pressure gradient region of transonic shock/boundary layer interaction by Bernardini *et al.* [4] They inferred that this behaviour is likely linked with large two-dimensional roller-type structures developing in the separated shear layer over the separation bubble. In the present study, we further discuss the enhanced spanwise coherence by inspecting the integral length scale in the separation region. The spanwise and streamwise integral length scales are respectively defined as

$$\Lambda_z(x_0) = \int_{-\infty}^{+\infty} |R_{\tau'_x \tau'_x}(x_0 : 0, \Delta z)| dz,$$

$$\Lambda_x(x_0) = \int_{-\infty}^{+\infty} |R_{\tau'_x \tau'_x}(x_0 : \Delta x, 0)| dx. \quad (7)$$

Under the above definition, the computed spanwise integral length at locations S1–S3 are $\Lambda_z = 0.46\delta^*$, $0.57\delta^*$, and $0.87\delta^*$, respectively, much smaller than those found by Bernardini *et al.*, [4] who stated that the spanwise integral length for wall-pressure fluctuations is in the range $4.68\delta^*$ to $15.6\delta^*$. Accordingly, the presence of large spanwise roller-type structures observed in the outer layer should not be the same cause of the spanwise elongated maps for the fluctuating WSS in our study.

Considering that the integral scales in both directions are very small, approximately $O(\delta^*)$, we hypothesise that the attendant small-scale separated flow patches inside the separation bubble, as previously found by Humble *et al.* [38] in SWTBLI flows, might be the primary mechanism. In the reattachment region, under the combined effects of increased streamwise and decreased spanwise coherence, the contours at locations R1–R3 gradually recover to be streamwise elongated again. This is strongly related to the reoccurrence of the streaky structures in the downstream region. In addition, it is worth pointing out that the two-point correlation of the streamwise WSS fluctuations in the interaction region very closely resembles the near-wall velocity correlations in the incompressible separated TBL of Na and Moin. [37] Unlike the streamwise component, it can be seen in Figure 15 that the contours for the spanwise component exhibit little qualitative differences at different stations. Throughout the interaction, although the spatial coherence in both directions is slightly increased due to the shock interaction, the streamwise elongated shape is still preserved, which can be attributed to the persistence of the aforementioned wave-like pattern. It is suggested that the structural foundation of the spanwise WSS fluctuations is qualitatively undisturbed by the shock interaction.

Figure 16(a) and (b) show the contours of the space–time correlation for the streamwise and spanwise WSS fluctuations, respectively. The space–time correlation coefficient

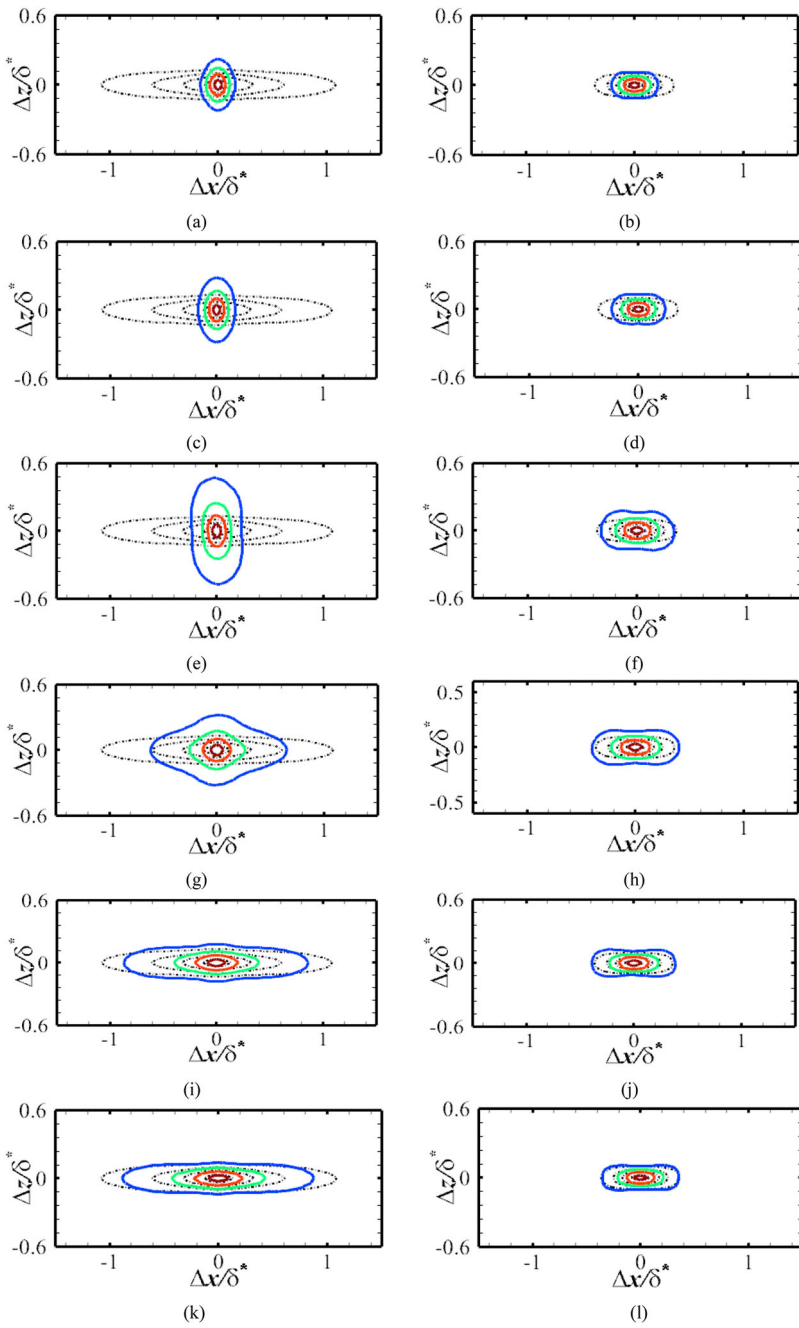


Figure 15. Iso-lines of the two-point correlation maps in the interaction region. Top to bottom: S1–R3; (a, c, e, g, i, k) streamwise component; (b, d, f, h, j, l) spanwise component. Four levels from 0.3 to 0.9 with increments of 0.2 are shown. Black dashed lines denote the results taken at x_{ref} .

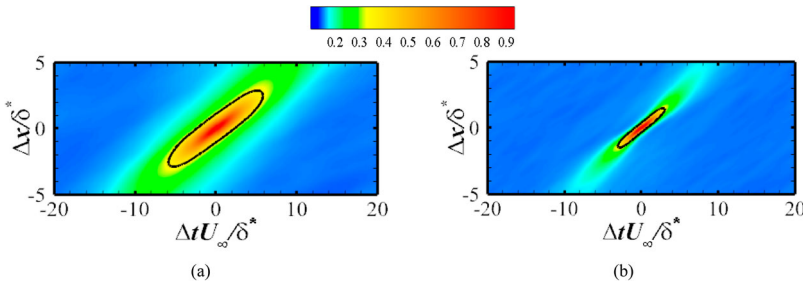


Figure 16. Contours of the space–time correlation for the fluctuating WSS at x_{ref} : (a) streamwise component τ_x' ; (b) spanwise component τ_z' . The solid lines denote a correlation value of 0.3.

is defined as

$$R_{\tau'\tau'}(x_0 : \Delta x, \Delta t) = \frac{\overline{\tau'(x_0, z, t)\tau'(x_0 + \Delta x, z, t + \Delta t)}}{\tau_{\text{rms}}(x_0)\tau_{\text{rms}}(x_0 + \Delta x)}, \quad (8)$$

where Δt is the time delay. Consistent with Jeon *et al.*, [11] since the WSS fluctuations are strongly propagated downstream, the contours for both components are highly skewed, exhibiting a narrowed forward-leaning elliptical behaviour with their major axes inclined in the direction of the first and third quadrants of the Δt – Δz plane. Clearly, the contour shape of the streamwise component is slightly wider than that of the spanwise component in the streamwise direction, due to relatively stronger streamwise coherence. Using a similar procedure to that described by Jeon *et al.* [11] and Duan *et al.*, [39] we estimate the convection velocity of the WSS fluctuations from the space–time correlation as

$$\left. \frac{\partial R_{\tau'\tau'}(x_0 : \Delta x, \Delta t)}{\partial \Delta x} \right|_{\Delta x = \Delta x_{pk}} = 0, \quad (9)$$

Here, the convection velocity U_c for a given time delay Δt is defined as the ratio $\Delta x_{pk}/\Delta t$, with Δx_{pk} corresponding to the spatial separation where the maximum correlation value is obtained. The computed convection velocities for both components at the reference station are reported in Figure 17 as a function of the time delay. Generally, for the streamwise component, the small-scale disturbances (i.e. short time delay) propagate at small speeds of $U_c \approx 0.43U_\infty$ – $0.48U_\infty$, whereas the large-scale disturbances (i.e. long time delay) propagate at a large speed of $U_c \approx 0.50U_\infty$ – $0.53U_\infty$. It can be seen in Figure 17 that the convection velocity distributions for the spanwise component are very similar to those of the streamwise component, the main difference being slightly larger speeds at longer time delays. The overall convection velocity for the streamwise component is about $U_c \approx 0.44U_\infty$, a little smaller than the speed of $U_c \approx 0.49U_\infty$ for the spanwise component. A similar trend was also observed by Jeon *et al.*, [11] who suggested that the corresponding speeds are $U_c \approx 0.53U_\infty$ and $U_c \approx 0.57U_\infty$, respectively. It is worth recalling that the Reynolds number in the DNS of Jeon *et al.* [11] is much lower than that in the present study. As pointed out by Daniel *et al.*, [13] the convection velocity slowly decreases with increasing Reynolds number.

In Figure 18, iso-lines of the space–time correlation maps for the WSS fluctuations at various streamwise locations in the interaction region are directly compared with those of the upstream TBL. Two clear observations can be made regarding the effect of the shock

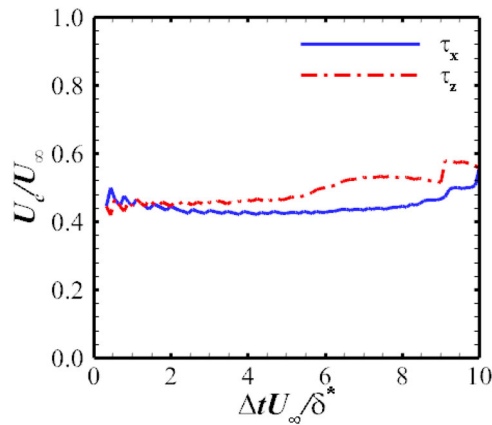


Figure 17. Convection velocity as a function of time delay at x_{ref} .

interaction on both components. First, we highlight that the contours are sharply contracted in the separation region as a consequence of the systematic reduction in the spatial and temporal extents. This means that the WSS fields significantly lose their coherence in SWTBLI flows, in accordance with the previous correlation results of the wall-pressure field in the separation bubble [2]. In the reattachment region, the contours appear to exhibit a slow recovery behaviour in which the extents in both directions are gradually increased. Taking the correlation level of 0.3 as an example, it is found that the temporal extents of the streamwise WSS fluctuations at locations S1 and R3 are about 31% and 87% shorter than that of the upstream TBL. However, it is confirmed that the contour shapes at all locations are characterised by a similar elliptic trend, indicating that the shock interaction exhibits little influence on the downstream propagation of the WSS fluctuation, despite the existence of a separation bubble. However, we note that the overall inclination of the correlation contour is greatly changed, which rotates relative to that of the upstream TBL. It can be seen that the angles between the major axes of the upstream TBL and those at each streamwise location experience an increase at locations S1–S3, followed by a decrease in the reattachment region. To be specific, for the streamwise fluctuation, the angles at locations S1, S3, and R3 are estimated to be about 17.6° , 20.4° , and 7.7° , respectively. With little doubt, the corresponding convection-velocity distribution in the interaction is expected to be significantly altered.

Regarding the shock interaction effect on the convection velocity shown in Figure 19, we observe that there are utterly different trends in the separation region and in the reattachment region. Clearly, the convection velocity decreases monotonically in the separation region, dropping to values in the range $0.05U_\infty$ to $0.1U_\infty$ at location S3 for both components. This is likely because the significantly small propagation speeds in the separation region are probably linked to the very-low-speed reversed flows in the near-wall region. Subsequently, in the reattachment region, it is seen that the convection velocities for both components start to increase persistently, which becomes more significant at long time separations (associated with large-scale disturbances). Specifically, at short time separation, the convection velocity for the streamwise WSS fluctuations is approximately $0.25U_\infty$ at location R3, whereas it varies between $0.3U_\infty$ and $0.5U_\infty$ at long time separations, which

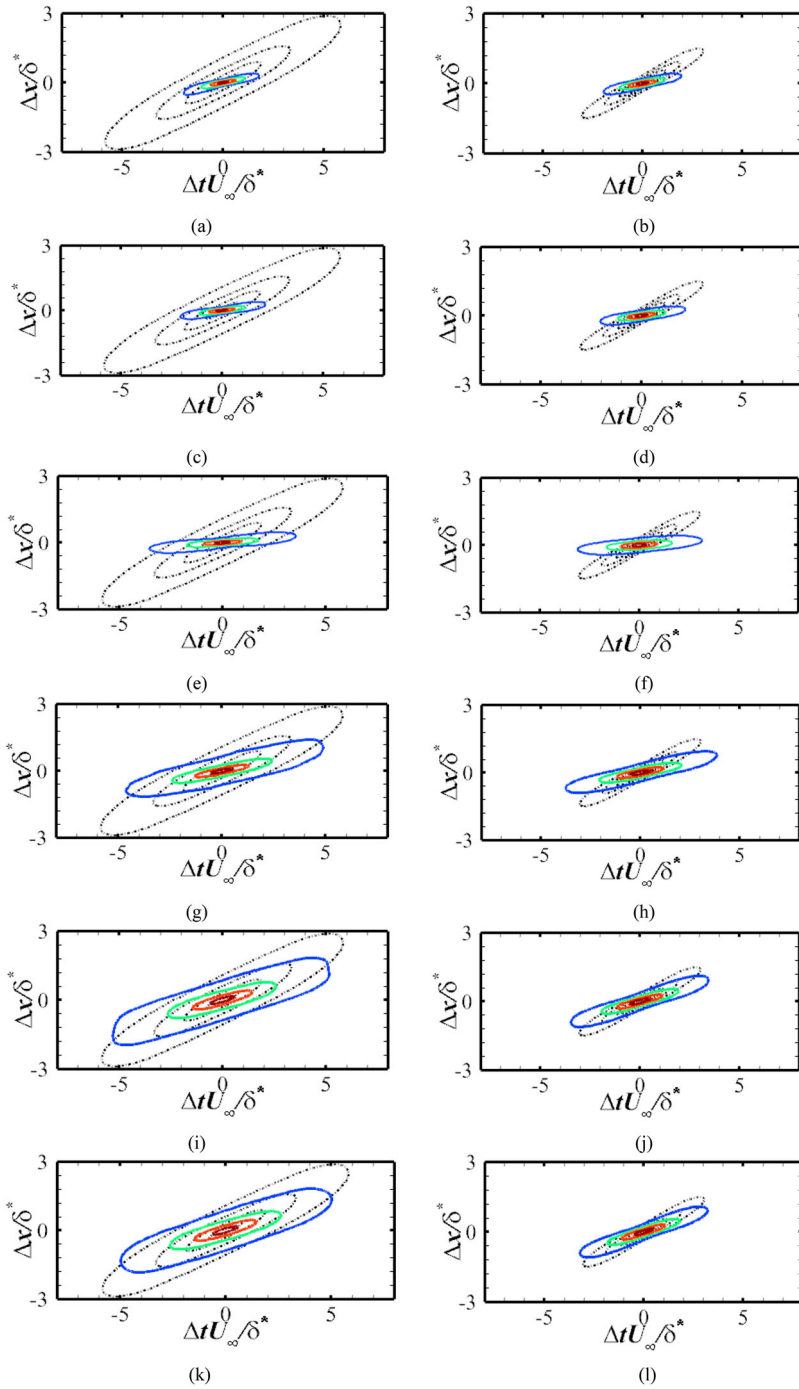


Figure 18. Iso-lines of the space–time correlation maps in the interaction region. Top to bottom: S1–R3; (a, c, e, g, i, k) streamwise component; (b, d, f, h, j, l) spanwise component. Four levels from 0.3 to 0.9 with increments of 0.2 are shown. Black dashed lines denote the results taken at x_{ref} .

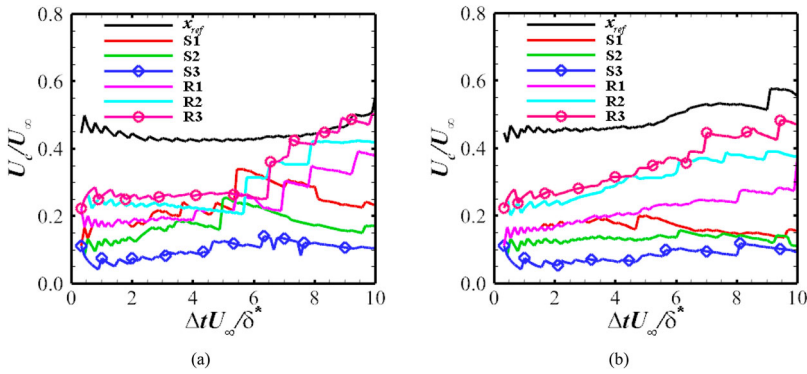


Figure 19. Distributions of convection velocity normalised by the free-stream velocity: (a) streamwise component τ_x ; (b) spanwise component τ_z .

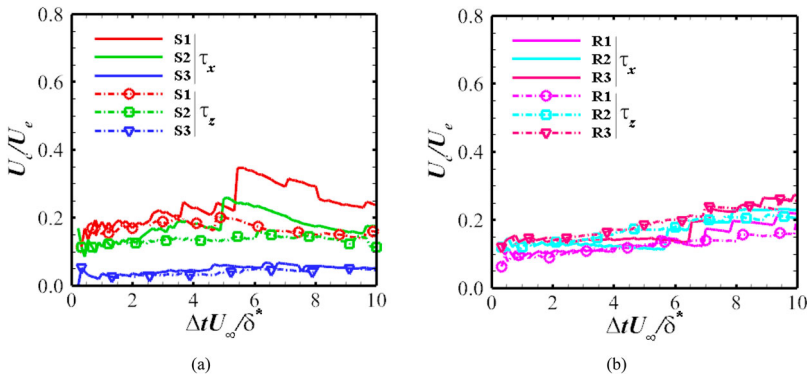


Figure 20. Distributions of convection velocity normalised by the local external velocity: (a) separation region; (b) reattachment region.

is very close to the upstream values. Given that the large-scale disturbances located farther away from the wall are mainly responsible for the convection speed for the wall-pressure fluctuations at long time separations, as suggested by Willmarth [40] and Bernardini and Pirozzoli [36], it is reasonable to speculate that this discrepancy in the propagation speed for the short and long time separations might be related to predominance of the large-scale structures redeveloping in the reattached boundary layer, as observed in the coherent vortex structures present in Figure 6 and the WSS fields in Figure 7.

Figure 20 shows the convection velocity normalised by the local external velocity U_e . It can be seen from Figure 20(a) that, for both the streamwise and spanwise components, no collapse of the normalised convection velocity distributions is found, suggesting that the outer scaling is not valid in the separation region. However, in the reattachment region, the normalised convection velocity exhibits less variation, leading to an approximate collapse of the distributions at locations R1–R3, as shown in Figure 20(b). It turns out that the convection velocities at short and long time separations are about $0.1U_e$ and $0.2U_e$, respectively.

4. Conclusions

In this study, the characteristics of the streamwise and spanwise WSS fluctuations in SWT-BLI on a flat plate at Mach 2.25 are investigated by means of DNS. A PDF analysis shows that the highly positively skewed profile of the streamwise fluctuations is significantly modified across the interaction, exhibiting roughly symmetric behaviour in the separation region, while the PDF shape of the spanwise fluctuations is slightly changed in the interaction when normalisation by the local rms value is applied. In contrast to the wall-pressure fluctuations in SWTBLI flows, the frequency spectra of the fluctuating WSS are very insensitive to the unsteady shock motion, and the low-frequency energy at the mean separation point is not significantly enhanced by the typical low-frequency unsteadiness. The characteristic frequencies for both components are mostly preserved throughout the interaction region. Two-point correlation analysis revealed an increase of the spanwise coherence associated with the streamwise component in the separation region, while the spanwise component is mainly dominated by the streamwise coherence throughout the interaction. The space–time correlations of the WSS fluctuations, which obey the classic elliptic trend, evidence a strong reduction of the propagation speed in the reversed flow. In the reattachment region, the local external velocity produces a better collapse of the convection velocity distribution, but it is not valid in the separation region.

Disclosure statement

No potential conflict of interest was reported by the author(s).

Funding

This study was co-supported by the National Natural Science Foundation of China (grant numbers 11972356 and 91852203) and the National Key R&D Program of China (grant number 2019YFA0405300).

ORCID

Xinliang Li  <http://orcid.org/0000-0002-4264-9620>

References

- [1] Clemens NT, Narayanaswamy V. Low-frequency unsteadiness of shock wave/turbulent boundary layer interactions. *Annu Rev Fluid Mech.* 2014;46:469–492.
- [2] Fang J, Zheltovodov AA, Yao YF, et al. On the turbulence amplification in shock-wave/turbulent boundary layer interaction. *J Fluid Mech.* 2020;897:A32.
- [3] Bonnet JP. Space-time correlations of wall pressure fluctuations in shock-induced separated turbulent flows. *Phys Fluids.* 1988;31:2821–2833.
- [4] Bernardini M, Pirozzoli S, Grasso F. The wall pressure signature of transonic shock/boundary layer interaction. *J Fluid Mech.* 2011;671:288–312.
- [5] Grosse S, Schröder W. Wall-shear stress patterns of coherent structures in turbulent duct flow. *J Fluid Mech.* 2009;633:147–158.
- [6] Brücker C. Signature of varicose wave packets in the viscous sublayer. *Phys Fluids.* 2008;20:061701.
- [7] Colella KJ, Keith WL. Measurements and scaling of wall shear stress fluctuations. *Exp Fluids.* 2003;34:253–260.

- [8] Nottebrock B, Geurts KJ, Schroder W. Wall-shear stress measurements in an adverse pressure gradient turbulent boundary layer. 7th AIAA Flow control conference 2014, Report No.: AIAA-2014-2098.
- [9] Wietrzak A, Lueptow RM. Wall shear stress and velocity in a turbulent axisymmetric boundary layer. *J Fluid Mech.* 1994;259:191–218.
- [10] Li YX, Naguib AM, Hudy LM. Two-point measurements of wall shear stress beneath an axisymmetric separating/reattaching flow. *AIAA J.* 2008;46(10):2649–2652.
- [11] Jeon S, Choi H, Yoo JY, et al. Space-time characteristics of the wall shear-stress fluctuations in a low-Reynolds number channel flow. *Phys Fluids.* 1999;11(10):3084–3094.
- [12] Hu ZW, Morfey CL, Sandham ND. Wall pressure and shear stress spectra from direct numerical simulations of channel flow up to $Re_\tau = 1440$. *AIAA J.* 2006;44(7):1541–1549.
- [13] Daniel CD, Laizet S, Vassilicos JC. Wall shear stress fluctuations: mixed scaling and their effects on velocity fluctuations in a turbulent boundary layer. *Phys Fluids.* 2017;29:055102.
- [14] Tong FL, Yu CP, Tang ZG, et al. Numerical studies of shock wave interactions with a supersonic turbulent boundary layer in compression corner: turning angle effects. *Comput Fluids.* 2017;149:56–69.
- [15] Tong FL, Li XL, Duan YH, et al. Direct numerical simulation of supersonic turbulent boundary layer subjected to a curved compression ramp. *Phys Fluids.* 2017;29:125101.
- [16] Tong FL, Li XL, Yuan XX, et al. Incident shock wave and supersonic turbulent boundary layer interactions near an expansion corner. *Comput Fluids.* 2020;198:104385.
- [17] Li XL, Fu DX, Ma YW. Direct numerical simulation of hypersonic boundary-layer transition over a blunt cone. *AIAA J.* 2008;46(11):2899–2913.
- [18] Martin MP, Taylor EM, Wu M, et al. A bandwidth-optimized WENO scheme for the effective direction numerical simulation of compressible turbulence. *J Comput Phys.* 2006;220:270–289.
- [19] Wu M, Martin MP. Direct numerical simulation of supersonic turbulent boundary layer over a compression ramp. *AIAA J.* 2007;45(4):879–889.
- [20] Pirozzoli S, Grasso F, Gatski TB. Direct numerical simulation and analysis of a spatially evolving supersonic turbulent boundary layer at $M = 2.25$. *Phys Fluids.* 2004;16(3):530–545.
- [21] Li XL, Fu DX, Ma YW. Direct numerical simulation of a spatially evolving supersonic turbulent boundary layer at $Ma = 6$. *Chin Phys Lett.* 2006;23(6):1519–1522.
- [22] Pirozzoli S, Bernardini M. Direct numerical simulation database for impinging shock wave/turbulent boundary-layer interaction. *AIAA J.* 2011;49(6):1307–1312.
- [23] Tong FL, Sun D, Li XL. Direct numerical simulation of impinging shock wave and turbulent boundary layer interaction over a wavy-wall. *Chinese J Aeronaut.* 2021;34(5):350–363.
- [24] Gao H, Fu DX, Ma YW, et al. Direct numerical simulation of supersonic turbulent boundary layer. *Chin Phys Lett.* 2005;22(7):1709–1712.
- [25] Guarini SE, Mose RD, Shariff K, et al. Direct numerical simulation of a supersonic turbulent boundary layer at Mach 2.5. *J Fluid Mech.* 2000;414:1–33.
- [26] Maeder T, Adams NA, Kleiser L. Direct simulation of turbulent supersonic boundary layers by an extended temporal approach. *J Fluid Mech.* 2001;429:187–216.
- [27] Schlatter P, Orlu R. Assessment of direct numerical simulation data of turbulent boundary layers. *J Fluid Mech.* 2010;659:116–126.
- [28] Pirozzoli S, Grasso F. Direct numerical simulation of impinging shock wave/turbulent boundary layer interaction at $M = 2.25$. *Phys Fluids.* 2006;18:065113.
- [29] Pirozzoli S, Bernardini M, Grasso F. Direct numerical simulation of transonic shock/boundary layer interaction under conditions of incipient separation. *J Fluid Mech.* 2010;657:361–393.
- [30] Li XL, Fu DX, Ma YW. Direct numerical simulation of shock/turbulent boundary layer interaction in a supersonic compression ramp. *Sci China Phys Mech Astron.* 2010;53(9):1651–1658.
- [31] Tong FL, Chen JQ, Sun D, et al. Wall-shear stress fluctuations in a supersonic turbulent boundary layer over an expansion corner. *J Turbul.* 2020;21(7):355–374.
- [32] Pasquariello V, Hickel S, Adams NA. Unsteady effects of strong shock-wave/boundary-layer interaction at high Reynolds number. *J Fluid Mech.* 2017;823:617–657.
- [33] Priebe S, Tu JH, Rowley CW, et al. Low-frequency dynamics in a shock-induced separated flow. *J Fluid Mech.* 2016;807:441–477.

- [34] Ringuette MJ, Bookey P, Wyckham C, et al. Experimental study of a Mach 3 compression ramp interaction at $Re_\theta = 2400$. *AIAA J.* **2009**;47(2):373–385.
- [35] Bernardini M, Asproulias I, Larsson J, et al. Heat transfer and wall temperature effects in shock wave turbulent boundary layer interactions. *Phys Rev Fluids.* **2016**;1:084403.
- [36] Bernardini M, Pirozzoli S. Wall pressure fluctuations beneath supersonic turbulent boundary layers. *Phys Fluids.* **2011**;23:085102.
- [37] Na Y, Moin P. The structure of wall-pressure fluctuations in turbulent boundary layers with adverse pressure gradient and separation. *J Fluid Mech.* **1998**;377:347–373.
- [38] Humble RA, Scarano F, Oudheusden BW. Unsteady aspects of an incident shock wave/turbulent boundary layer interaction. *J Fluid Mech.* **2009**;635:47–74.
- [39] Duan L, Choudhari MM, Zhang C. Pressure fluctuations induced by a hypersonic turbulent boundary layer. *J Fluid Mech.* **2016**;804:578–607.
- [40] Willmarth WW. Wall pressure fluctuations beneath turbulent boundary layer. *Annu Rev Fluid Mech.* **1975**;7:13–36.